*Inorg. Chem.* **2004**, *43*, 3067–3079


# A Structural and Mössbauer Study of Complexes with $Fe_2(\mu\text{-}O(H))_2$ Cores: Stepwise Oxidation from $Fe^{II}(\mu\text{-}OH)_2Fe^{II}$ through $Fe^{II}(\mu\text{-}OH)_2Fe^{III}$ to $Fe^{III}(\mu\text{-}O)(\mu\text{-}OH)Fe^{III}$

**Audria Stubna,[†] Du-Hwan Jo,[‡] Miquel Costas,[‡] William W. Brenessel,[‡] Hanspeter Andres,[†] Emile L. Bominaar,[†] Eckard MUnck,*[,†] and Lawrence Que, Jr.*[,‡]**

*Department of Chemistry, Carnegie Mellon University, 4400 Fifth Avenue, Pittsburgh, Pennsylvania 15213, and Department of Chemistry and Center for Metals in Biocatalysis, 207 Pleasant Street SE, University of Minnesota, Minneapolis, Minnesota 55455*

Received October 13, 2003

Dinuclear non-heme iron clusters containing oxo, hydroxo, or carboxylato bridges are found in a number of enzymes involved in $O_2$ metabolism such as methane monooxygenase, ribonucleotide reductase, and fatty acid desaturases. Efforts to model structural and/or functional features of the protein-bound clusters have prompted the preparation and study of complexes that contain $Fe(\mu\text{-}O(H))_2Fe$ cores. Here we report the structures and spectroscopic properties of a family of diiron complexes with the same tetradentate N4 ligand in one ligand topology, namely $[(\alpha\text{-BPMCN})_2Fe^{II}_2(\mu\text{-OH})_2](CF_3SO_3)_2$ (**1**), $[(\alpha\text{-BPMCN})_2Fe^{II}Fe^{III}(\mu\text{-OH})_2](CF_3SO_3)_3$ (**2**), and $[(\alpha\text{-BPMCN})_2Fe^{III}_2(\mu\text{-O})(\mu\text{-OH})](CF_3SO_3)_3$ (**3**) (BPMCN = *N,N′*-dimethyl-*N,N′*-bis(2-pyridylmethyl)-*trans*-1,2-diaminocyclohexane). Stepwise one-electron oxidations of **1** to **2** and then to **3** demonstrate the versatility of the $Fe(\mu\text{-}O(H))_2Fe$ diamond core to support a number of oxidation states with little structural rearrangement. Insight into the electronic structure of **1**, **2′**, and **3** has been obtained from a detailed Mössbauer investigation (**2′** differs from **2** in having a different complement of counterions). Mixed-valence complex **2′** is ferromagnetically coupled, with $J = -15 \pm 5$ cm$^{-1}$ ($H = J\mathbf{S}_1\cdot\mathbf{S}_2$). For the $S = {}^9/_2$ ground multiplet we have determined the zero-field splitting parameter, $D_{9/2} = -1.5 \pm 0.1$ cm$^{-1}$, and the hyperfine parameters of the ferric and ferrous sites. For $T < 12$ K, the $S = {}^9/_2$ multiplet has uncommon relaxation behavior. Thus, $M_S = -{}^9/_2 \leftrightarrow M_S = +{}^9/_2$ ground state transition is slow while $\Delta M_S = \pm 1$ transitions between equally signed $M_S$ levels are fast on the time scale of Mössbauer spectroscopy. Below 100 K, complex **2′** is trapped in the $Fe_1^{III}Fe_2^{II}$ ground state; above this temperature, it exhibits thermally assisted electron hopping into the state $Fe_1^{II}Fe_2^{III}$. The temperature dependence of the isomer shifts was corrected for second-order Doppler shift, obtained from the study of diferrous **1**. The resultant true shifts were analyzed in a two-state hopping model. The diferric complex **3** is antiferromagnetically coupled with $J = 90 \pm 15$ cm$^{-1}$, estimated from a variable-temperature Mössbauer analysis.

## Introduction

Oxo- or hydroxo-bridged non-heme diiron centers are structural motifs commonly found among proteins involved in $O_2$ metabolism such as hemerythrin, the hydroxylase component of methane monooxygenase (MMOH), the R2 subunit of class 1 ribonucleotide reductases (RNR R2), and fatty acid desaturases.[1−4] Efforts to model these proteins from structural and/or functional points of view have stimulated the study of complexes containing $Fe(\mu\text{-}O(H))_2Fe$ cores.[5] Molecules containing $Fe^{II}(\mu\text{-}OH)_2Fe^{II}$ units have been obtained to model the reduced state of the enzymes and exhibit reactivity toward $O_2$.[6−8] The only example of a complex containing the $Fe^{II}(\mu\text{-}OH)_2Fe^{III}$ core has very recently been

* To whom correspondence should be addressed. E-mail: emunck@cmu.edu (E.M.); que@chem.umn.edu (L.Q.). Fax: 412-268-1061 (E.M.); 612-624-7029 (L.Q.).
[†] Carnegie Mellon University.
[‡] University of Minnesota.

(1) Kurtz, D. M., Jr. *Chem. Rev.* **1990**, *90*, 585−606.
(2) Wallar, B. J.; Lipscomb, J. D. *Chem. Rev.* **1996**, *96*, 2625−2657.
(3) Solomon, E. I.; Brunold, T. C.; Davis, M. I.; Kemsley, J. N.; Lee, S.-K.; Lehnert, N.; Neese, F.; Skulan, A. J.; Yang, Y.-S.; Zhou, J. *Chem. Rev.* **2000**, *100*, 235−349.
(4) Merkx, M.; Kopp, D. A.; Sazinsky, M. H.; Blazyk, J. L.; Muller, J.; Lippard, S. J. *Angew. Chem., Int. Ed.* **2001**, *40*, 2782−2807.

10.1021/ic030296k CCC: $27.50 
Published on Web 04/14/2004

described[9] and is closely related to the mixed-valence $Fe^{II}$-($\mu$-OH)($\mu$-$OH_2$)$Fe^{III}$ form of MMOH.[10,11] Corresponding $Fe^{III}$-$Fe^{III}$ complexes have Fe($\mu$-O)($\mu$-OH)Fe cores owing to the Lewis acidity of the iron(III) centers; examples of such complexes have been described by us and others.[12−15] Crystallographic information for complexes containing $Fe^{III}$($\mu$-$O)_2Fe^{III}$ and $Fe^{III}$($\mu$-$O)_2Fe^{IV}$ cores is also available,[5,13,16] and a model compound containing an $Fe^{IV}$($\mu$-$O)_2Fe^{IV}$ diamond core structure has been spectroscopically characterized.[17] These highly reactive molecules constitute synthetic precedents for the high valent $Fe^{III}Fe^{IV}$ intermediate **X** of RNR R2[18] and the $Fe^{IV}$($\mu$-$O)_2Fe^{IV}$ diamond core structure suggested for intermediate **Q** in MMOH.[19]

The high versatility of an oxo/hydroxo-bridged dimetal core arises from its ability to modulate its properties by simple protonation or deprotonation, allowing enzymes a simple way to control the redox potential and oxidation state of intermediates in their catalytic cycles. In this work, we report the synthesis and X-ray structural characterization of a family of three oxo/hydroxo-bridged diiron complexes, namely [(α-BPMCN)$_2Fe^{II}_2$($\mu$-$OH)_2$]($CF_3SO_3)_2$ (**1**), [(α-BPMCN)$_2Fe^{II}Fe^{III}$($\mu$-$OH)_2$]($CF_3SO_3)_3$ (**2**), and [(α-BPMCN)$_2Fe^{III}_2$($\mu$-O)($\mu$-OH)]($CF_3SO_3)_3$ (**3**), and examine the effect of stepwise one-electron oxidations on the properties of the diiron core. This work further illustrates the high versatility of the Fe($\mu$-O(H))$_2$Fe diamond core structure to support a number of oxidation states with little structural rearrangement. We have also studied **1**, **2′**, and **3** in detail with Mössbauer spectroscopy, focusing in particular on the $Fe^{II}Fe^{III}$ mixed-valence state of **2′**;[20,21] the latter differs from **2** by having a different complement of counterions. Complex **2′** is valence-localized below 100 K and exhibits well-resolved Mössbauer spectra with uncommon relaxation properties at low temperature, allowing us to determine the zero-field splittings of the $S = {}^9/_2$ ground multiplet, the exchange coupling constant $J$, and the hyperfine parameters of both iron sites. At temperatures above 100 K, complex **2′** undergoes thermal assisted electron hopping.

## Experimental Section

**Materials and Synthesis.** All reagents were purchased from commercial sources and used as received, unless noted otherwise. $CH_3CN$ and diethyl ether were purified by passing through alumina purification columns, and $CH_2Cl_2$ was distilled from $CaH_2$. Solvents were degassed by several Ar−vacuum cycles and stored in an anaerobic glovebox. Preparation and handling of air-sensitive materials were carried out under an argon atmosphere using standard Schlenk techniques or in an anaerobic glovebox.

**[(α-BPMCN)$_2Fe^{II}_2$($\mu$-$OH)_2$]($CF_3SO_3)_2$ (1).** To a solution of [(α-BPMCN)$Fe^{II}$($CF_3SO_3)_2$] (1.19 g, 1.75 mmol) in $CH_3CN$ (10 mL) was added a $CH_3OH$ (5 mL) solution of NaOH (78 mg, 1.95 mmol), and the mixture was stirred overnight. The solution was dried in vacuo, and the residue was redissolved in $CH_2Cl_2$ (20 mL). After filtration to remove $NaCF_3SO_3$, the filtrate was dried under vacuum. The orange residue was recrystallized from $CH_2Cl_2$/ether to obtain the product as an orange microcrystalline solid (yield 698 mg, 73%). [(α-(*R*,*R*)-BPMCN)$_2Fe^{II}_2$($\mu$-$OH)_2$]($CF_3SO_3)_2$ was prepared in an analogous way by starting with [(α-(*R*,*R*)-BPMCN)$Fe^{II}$($CF_3SO_3)_2$]. Anal. Calcd (Found) for $C_{42}H_{58}F_6Fe_2N_8O_8S_2$: %C, 46.16 (46.05); %H, 5.35 (5.15); %N, 10.25 (10.25); %S, 5.87 (5.73). $^1$H NMR ($\delta$, ppm, $CD_3CN$): 119.3 (4H), 105.2 (4H), 66.4 (12H), 48.8 (4H), 39.3 (4H), 38.7 (4H), 21.3 (4H), 14.1 (4H), 11.9 (4H), 11.0 (8H), −36.2 (4H). UV−vis ($CH_2Cl_2$): $\lambda_{max}$ ($\epsilon$) = 450 nm (3300 $M^{-1}$ $cm^{-1}$). EPR (parallel mode, $CH_2Cl_2$ at 8 K): $g \approx 16$.

**[(α-BPMCN)$_2Fe^{II}Fe^{III}$($\mu$-$OH)_2$]($CF_3SO_3)_3$ (2).** Solid $AgCF_3SO_3$ (21 mg, 0.08 mmol) was added to a precooled (−80 °C) $CH_2Cl_2$ (10 mL) solution of **1** (100 mg, 0.09 mmol), and the mixture was stirred at this temperature for 2 h. At this time, the mixture was warmed and filtered. The residue was washed with $CH_2Cl_2$/$CH_3CN$ (5:1) (5 mL), and the filtrates were combined. Ether (15 mL) was quickly added to the combined filtrates to yield a gray solid, which was recrystallized by diffusion of ether into a $CH_2Cl_2$ solution to afford the product as pale green crystals (91 mg, 80%). From this procedure, diffraction quality crystals of **2** were obtained; the crystal structure obtained from this batch showed an ordered $Fe^{II}$-$Fe^{III}$($\mu$-$OH)_2$ core and is thus presented in this paper. Anal. Calcd (Found) for $C_{43}H_{58}F_9Fe_2N_8O_{11}S_3 \cdot H_2O$: %C, 40.99 (41.22); %H, 4.80 (4.95); %N, 8.89 (8.64); %S, 7.75 (7.06). $^1$H NMR ($\delta$, ppm, $CD_2Cl_2$): 279.5 (4H), 179.8 (12H), 161.9 (4H), 90.0 (4H), 83.9 (4H), 77.5 (4H), 52.8 (4H), 28.8 (4H), 26.9 (8H), −1.0 (4H), −5.9 (4H). UV−vis ($CH_2Cl_2$): $\lambda_{max}$ ($\epsilon$) = 750 nm (300 $M^{-1}$ $cm^{-1}$). Alternatively, [Fe(Cp)$_2$]($PF_6$) (0.331 g, 1.0 mmol) could also be used as oxidant when added to a $CH_2Cl_2$ solution (15 mL) of **1** (1.092 g, 1.0 mmol) and stirred for 2 h at room temperature. The resulting yellow-brown solution was filtered and layered with diethyl ether to afford brown crystals (yield 1.056 g, 85%). This sample, designated **2′**, and formulated as [(α-BPMCN)$_2Fe^{II}Fe^{III}$($\mu$-$OH)_2$]($CF_3SO_3)_2$($PF_6$), was used for the detailed Mössbauer studies reported in this paper.

**[(α-BPMCN)$_2Fe^{III}_2$($\mu$-O)($\mu$-OH)]($CF_3SO_3)_3$ (3).** To a solution of **1** (100 mg, 0.09 mmol) in $CH_3CN$ (3 mL) was added a $CH_3CN$ (3 mL) solution of $AgCF_3SO_3$ (47 mg, 0.18 mmol), and the mixture was stirred for 30 min. After filtration, the filtrate was treated with ether (15 mL) to precipitate a brown solid that was isolated by


(5) Que, L., Jr.; Tolman, W. B. *Angew. Chem., Int. Ed.* **2002**, *41*, 1114−1137.
(6) MacMurdo, V. L.; Zheng, H.; Que, L., Jr. *Inorg. Chem.* **2000**, *39*, 2254−2255.
(7) Hikichi, S.; Ogihara, T.; Fujisawa, K.; Kitajima, N.; Akita, M.; Morooka, Y. *Inorg. Chem.* **1997**, *36*, 4539−4547.
(8) Kitajima, N.; Tamura, N.; Tanaka, M.; Morooka, Y. *Inorg. Chem.* **1992**, *31*, 3342−3343.
(9) Egdal, R. K.; Hazell, A.; Larsen, F. B.; McKenzie, C. J.; Scarrow, R. C. *J. Am. Chem. Soc.* **2003**, *125*, 32−33.
(10) Whittington, D. A.; Lippard, S. J. *J. Am. Chem. Soc.* **2001**, *123*, 827−838.
(11) Hendrich, M. P.; Münck, E.; Fox, B. G.; Lipscomb, J. D. *J. Am. Chem. Soc.* **1990**, *112*, 5861−5865.
(12) Zang, Y.; Pan, G.; Que, L., Jr.; Fox, B. G.; Münck, E. *J. Am. Chem. Soc.* **1994**, *116*, 3653−3654.
(13) Zheng, H.; Zang, Y.; Dong, Y.; Young, V. G., Jr.; Que, L., Jr. *J. Am. Chem. Soc.* **1999**, *121*, 2226−2235.
(14) Poussereau, S.; Blondin, G.; Cesario, M.; Guilhem, J.; Chottard, G.; Gonnet, F.; Girerd, J.-J. *Inorg. Chem.* **1998**, *37*, 3127−3132.
(15) Poussereau, S.; Blondin, G.; Chottard, G.; Guilhem, J.; Tchertanov, L.; Riviere, E.; Girerd, J.-J. *Eur. J. Inorg. Chem.* **2001**, 1057−1062.
(16) Hsu, H.-F.; Dong, Y.; Shu, L.; Young, V. G., Jr.; Que, L., Jr. *J. Am. Chem. Soc.* **1999**, *121*, 5230−5237.
(17) Costas, M.; Rohde, J.-U.; Stubna, A.; Ho, R. Y. N.; Quaroni, L.; Münck, E.; Que, L., Jr. *J. Am. Chem. Soc.* **2001**, *123*, 12931−12932.
(18) Riggs-Gelasco, P. J.; Shu, L.; Chen, S.; Burdi, D.; Huynh, B. H.; Que, L., Jr.; Stubbe, J. *J. Am. Chem. Soc.* **1998**, *120*, 849−860.
(19) Shu, L.; Nesheim, J. C.; Kauffmann, K.; Münck, E.; Lipscomb, J. D.; Que, L., Jr. *Science* **1997**, *275*, 515−518.
(20) Complex **2′** was obtained by oxidation of **1** with 1 equiv of [Fe(Cp)$_2$]($PF_6$). As the mixed-valence complex requires three counterions, **2′** is most likely [(α-BPMCN)$_2Fe^{II}Fe^{III}$($\mu$-$OH)_2$]($CF_3SO_3)_2$($PF_6$).
(21) Orville, A. M.; Lipscomb, J. D. *J. Biol. Chem.* **1993**, *268*, 8596−8607.

**Table 1.** Selected Bond Lengths (Å) and Bond Angles (deg) for **1**, **2**, and **3**

| | **1** | | **2** | | **3** | |
|---|---|---|---|---|---|---|
| | Fe1 | Fe2 | Fe1 | Fe2 | Fe1 | Fe2 |
| Fe−$\mu$-O(H) | 2.050(2) (O1) | 2.075(2) (O1) | 2.084(2) (O1) | 1.895(2) (O1) | 1.866(2) (O1) | 1.870(2) (O1) |
| | 2.080(2) (O2) | 2.036(2) (O2) | 2.082(2) (O2) | 1.897(2) (O2) | 1.989(2) (O2) | 1.998(2) (O2) |
| Fe−$N_{amine}$ | 2.283(3) (N1) | 2.282(3) (N5) | 2.242(3) (N1) | 2.206(3) (N5) | 2.181(3) (N2) | 2.178(3) (N6) |
| | 2.291(2) (N2) | 2.249(2) (N6) | 2.235(3) (N2) | 2.216(3) (N6) | 2.250(3) (N3) | 2.233(3) (N7) |
| Fe−$N_{py}$ | 2.220(3) (N3) | 2.206(3) (N7) | 2.184(3) (N3) | 2.168(3) (N7) | 2.170(2) (N1) | 2.175(3) (N5) |
| | 2.215(3) (N4) | 2.222(3) (N8) | 2.196(3) (N4) | 2.170(3) (N8) | 2.154(3) (N4) | 2.176(3) (N8) |
| Fe1−Fe2 | 3.048 | | 3.023 | | 2.867 | |
| ∠Fe1O1Fe2 | 95.26(9)° | | 98.78(10)° | | 100.24(10)° | |
| ∠Fe1O2Fe2 | 95.52(9)° | | 98.78(10)° | | 91.97(9)° | |

filtration and then dried under vacuum. Recrystallization by diffusion of ether into a $CH_3CN$ solution afforded the product as dark brown blocks (79 mg, 70%). Anal. Calcd (Found) for $C_{43}H_{57}F_9Fe_2N_8O_{11}S_3$: %C, 41.62 (41.32); %H, 4.63 (4.86); %N, 9.03 (8.86); %S, 7.75 (7.59). $^1$H NMR ($\delta$, ppm, $CD_3CN$): 81.0 (4H), 57.5 (4H), 54.2 (12H), 38.9 (4H), 28.8 (4H), 27.6 (4H), 25.1 (4H), 23.5 (4H), 7.3 (4H), 6.4 (4H), 4.7 (4H), −1.3 (4H). UV−vis ($CH_3CN$): $\lambda_{max}$ ($\epsilon$) = 588 nm (1600 $M^{-1}$ $cm^{-1}$). As mentioned in the synthesis of **2**, **3** can also be obtained by air oxidation of **1**.

**[(α-BPMEN)$_2$Fe$^{II}$Fe$^{III}$($\mu$-OH)$_2$](CF$_3$SO$_3$)$_3$ (4).** A $CH_2Cl_2$ solution of BPMEN (0.270 g, 1.0 mmol) was added to a $CH_2Cl_2/CH_3CN$ (5:1) solution (15 mL) of $Fe(CF_3SO_3)_2 \cdot 2CH_3CN$ (0.436 g, 1.0 mmol) and stirred for 10 min. Some $H_2O$ (0.018 g, 1.0 mmol) was slowly added to this solution and stirred for 2 h. The resulting yellow-orange solution was layered with aerobic diethyl ether to afford brown crystals (yield 0.453 g, 40%). Anal. Calcd (Found) for **4**, $C_{35}H_{46}F_9Fe_2N_8O_{11}S_3$: %C, 47.68 (47.56); %H, 5.60 (5.48); %N, 9.88 (9.90); %S, 8.49 (8.42).

**Physical Methods.** Electronic absorption spectra were recorded in quartz cuvettes on a Hewlett-Packard 8452 diode array spectrophotometer (190−820 nm scan range). $^1$H NMR spectra were recorded on Varian VXR-300 and VXR-500 spectrometers at room temperature. All spectra were obtained using a 90° pulse with 16 K data points. Chemical shifts for complexes (in ppm) were referenced to the residual protic solvent peak.

EPR spectra of **1** were collected at X-band microwave frequency with 100-kHz field modulation using a Bruker Elexsys E500 spectrometer. Cryotemperature was achieved with an Oxford Instruments ESR-10 continuous flow liquid helium cryostat and a digitalized temperature controller. Electrochemical measurements were performed at −40 °C (scan rate 50 mV/s) in $CH_2Cl_2$ with 0.1 M $Bu_4NBF_4$ as the supporting electrolyte using a BAS-100 electrochemical analyzer with a three-component system consisting of a Pt disk working electrode, a Pt wire auxiliary electrode, and a Ag wire as the reference electrode. The potential was referenced with ferrocene as the external standard.

Mössbauer spectra were recorded in two spectrometers that allowed measurements at temperatures between 1.5 and 240 K in parallel applied magnetic fields up to 8.0 T. The spectra were analyzed using the software WMOSS (WEB Research Co., Edina, MN).

**Crystallographic Studies.** Crystals suitable for X-ray diffraction were grown by vapor diffusion of ether into $CH_3CN$ (**1**) or $CH_2Cl_2$ (**2**) solutions of the complex. Crystals of **3** (containing a mixture of $ClO_4$ and $CF_3SO_3$ as counterions) were grown by vapor diffusion of ether into a $CH_3CN$ solution of **3** containing 1 equiv of $Bu_4NClO_4$. The crystals were attached to a glass fiber and mounted on a Bruker SMART system for data collection at 293(2) (**1**) or 173(2) K (**2** and **3**). An initial set of cell constants was calculated from reflections harvested from three sets of 20 frames. These initial sets of frames are oriented such that orthogonal wedges of reciprocal space were surveyed. This produces orientation matrices determined from 45 (**1**), 264 (**2**), and 350 (**3**) reflections. Final cell constants are calculated from the *xyz* centroids of 4743 (**1**), 8180 (**2**), 1010 (**3**) strong reflections from actual data collection. Crystallographic data are summarized in Table 1. Structures were solved using SHELXS-86 and refined using SHELXL-97.[22] Space groups were determined on the basis of systematic absences and intensity statistics. Direct-method solutions were calculated, providing most non-hydrogen atoms from the E-map. Full-matrix least-squares/difference Fourier cycles were performed that located the remaining non-hydrogen atoms. All non-hydrogen atoms were refined with anisotropic displacement parameters. All hydrogen atoms were placed in ideal positions and refined as riding atoms with individual (or group when appropriate) isotropic displacement parameters. In **1**, two of the triflate counterions, those containing S2 and S3, occupy their positions only 50% of the time per iron dimer, and the third, that containing S1, is fully occupied. The triflate containing S1 is disordered over two positions (67:33). In the case of the triflate containing S2, a nearby crystallographic inversion center produces the other position in the unit cell. This causes the problem that there is a void space for the 50% of the time when the triflate is in the other position, and vice versa. This void space, as determined by PLATON,[23] is approximately 165 Å$^3$ and holds approximately 14 electrons which is likely a water or acetonitrile molecule. Although some residual peaks of electron density were present (the largest is 1.71 electrons per Å$^3$), no definitive placement of solvent molecules could be made. The other half-occupied triflate site has an inversion center between the S3 and C43, and is thus disordered (50:50). The final full-matrix least-squares refinement converged to R1 = 0.0606 and wR2 = 0.2112 ($F^2$, all data). In **2**, one triflate molecule is disordered over two major sites (55:45). Remaining electron density in the vicinity of the disordered triflate molecule suggests further minor disorder, probably with a third site of the triflate molecule. This disorder could not be modeled. The packing of the molecules results in large voids containing disordered solvent molecules which could not be located. An investigation of the void space of the structure showed that 67 electrons are located in a major void of approximately 560 Å$^3$. The difference Fourier map, however, did not locate minor sites of the expected solvents (acetonitrile, ether, or dichloromethane). The data set was corrected for disordered solvent using the program PLATON/SQUEEZE.[23] The refinement using the corrected data set improved the overall structure and the R1 value by 1.5%. The final full-matrix least-squares refinement converged to R1 = 0.0417 and wR2 = 0.0994 (all data). In **3**, there is a counterion compositional disorder ($ClO_4/CF_3SO_3$) over two sites (74:26 and 19:81). Very likely these disorders are paired such that the volume of the two sites remains constant; however, disorder over three

(22) Sheldrick, G. M. *Acta Crystallogr., Sect. A* **1990**, *46*, 467−473.
(23) Spek, A. L. *PLATON. A multipurpose crystallographic tool*; Utrecht University: Utrecht, The Netherlands, 2002.

positions in a third anion (solely perchlorate 46:21:33) makes it difficult to be certain of the former statement. Two acetonitrile solvent molecules are also present, one of which is slightly disordered but could not be modeled as such. The final full-matrix least-squares refinement converged to R1 = 0.0377 and wR2 = 0.1017 ($F^2$, all data).

## Results

The reaction of [(α-BPMCN)$Fe^{II}(CF_3SO_3)_2$][24] with NaOH in MeOH affords after workup [(α-BPMCN)$_2Fe^{II}_2(\mu$-OH)$_2$]$(CF_3SO_3)_2$, **1**, as a crystalline, highly oxygen-sensitive orange solid in 73% yield. Cyclic voltammetry of **1** in $CH_2Cl_2$ shows a chemically reversible ($I_{pc}/I_{pa} = 1$) and electrochemically quasireversible ($\Delta E = 100$ mV) one-electron oxidation at $E_{1/2} = -360$ mV versus $Fc^+$/Fc to an $Fe^{II}Fe^{III}$ complex, and a further irreversible oxidation (loss of proton, see below) to an $Fe^{III}Fe^{III}$ complex is observed at + 650 mV. Low-temperature one-electron oxidation of **1** in $CH_2Cl_2$ with 0.9 equiv of $AgCF_3SO_3$ affords pale gray-green [(α-BPMCN)$_2Fe^{II}Fe^{III}(\mu$-OH)$_2$]$(CF_3SO_3)_3$, **2**, in 80% yield. Although indefinitely stable in $CH_2Cl_2$, the complex decomposes in the presence of coordinating solvents such as $CH_3CN$ or acetone. Reaction of **1** with 2 equiv of $AgCF_3SO_3$ affords, after workup, **3** as a brown-red solid in 70% yield.

**Description of the Solid Structures.** The availability of the diiron series **1**, **2**, and **3** represents a unique opportunity to study the effect of stepwise one-electron oxidation starting with the $Fe^{II}(\mu$-OH)$_2Fe^{II}$ core. Both ligand topology and the symmetry of the complex remain unaltered by oxidation (vide infra). The cationic part of **1** has a pseudo-$C_2$ axis perpendicular to the Fe$_2(\mu$-OH)$_2$ core and a second pseudo-$C_2$ axis along the Fe−Fe vector. Differences in bond distances lower the symmetry of the molecule (see also the Mössbauer spectra in Figure 3 which indicate two distinct sites). There is one severely disordered $CF_3SO_3^-$ group 3.0 Å from a bridging OH group, suggesting a hydrogen bonding interaction, although this does not cause significant distortion of the Fe−$\mu$-OH−Fe metrical parameters. When considered, the presence of this H-bonded $CF_3SO_3^-$ group eliminates the two $C_2$ axes of symmetry. For each iron atom, one of the Fe−OH bonds is slightly longer than the other ($\Delta r_{Fe-O}$ = 0.03−0.04 Å) resulting in some deformation of the diamond core. The magnitude of this deformation, however, is much smaller than the one observed in [(6-$Me_3$-TPA)$_2$-$Fe^{II}_2(\mu$-OH)$_2$]$(ClO_4)_2$ ($\Delta r_{Fe-O} = 0.2$ Å)[6] (6-$Me_3$-TPA = tris-(6-methyl-2-pyridylmethyl)amine), probably due to the fact that in **1** both hydroxo groups bind *trans* to equivalent aliphatic amines while in the latter they are bound *trans* to a pyridine and an aliphatic amine, respectively. The average Fe−OH distance of 2.06 Å compares well with those of previously reported complexes containing the Fe$_2(\mu$-OH)$_2$ core.[6−8] The core has average Fe−O−Fe angles of 95.4-(2)°, and the 3.048 Å Fe−Fe distance that results is the shortest thus far observed for such a complex. Average Fe−$N_{py}$ distances are slightly shorter than the corresponding Fe−$N_{amine}$ distances.

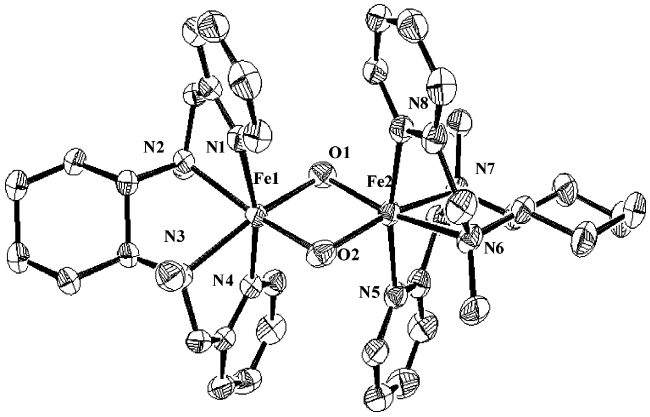


**Figure 1.** ORTEP plot (50% probability ellipsoids) of the cation of **2**.

Complex **2** is only the second example of a crystallographically characterized valence-localized $Fe^{II}Fe^{III}$ complex containing the Fe$_2(\mu$-OH)$_2$ core. This structure (Figure 1) displays parameters that allow us to distinguish between the $Fe^{II}$ and the $Fe^{III}$ centers which is in agreement with the Mössbauer spectroscopic results to be discussed below. In contrast, the recently reported crystal structure for the related [(α-BPMEN)$_2Fe^{II}Fe^{III}(\mu$-OH)$_2$]$(ClO_4)_3$ [BPMEN = *N*,*N*′-dimethyl-*N*,*N*′-bis(2-pyridylmethyl)-ethane-1,2-diamine] shows a diiron core with positional disorder so that the iron(II) and iron(III) ions could not be distinguished.[9] The average Fe1−$\mu$-OH and Fe2−$\mu$-OH distances listed in Table 1 (2.083 and 1.896 Å, respectively) for **2** correspond to those found for respective Fe−$\mu$-OH bonds in diiron(II)[6−8] and diiron(III) complexes,[12−15] and are in very good agreement with the values for [(α-BPMEN)$_2Fe^{II}Fe^{III}(\mu$-OH)$_2$]$(ClO_4)_3$ derived from EXAFS analysis.[9] The Fe−N bond lengths, on the other hand, are rather insensitive to the iron oxidation state; the average Fe2−N bond length is shorter by only ∼0.02 Å. Also, the Fe−Fe distance of 3.023 Å is only 0.025 Å shorter than that found in **1**. Thus, the one-electron oxidation of **1** does not result in a significant structural change, except for the large decrease in the lengths of the $Fe^{III}$−$\mu$-OH bonds. Finally, the two triflate counterions are H-bonded to the two hydroxide groups, with the $CF_3SO_3$ groups adopting monodentate ($d_{O(1)-O(6)} = 2.730(3)$ Å) and bidentate ($d_{O(2)-O(3)} = 3.030(4)$ Å and $d_{O(2)-O(5)} = 3.067(4)$ Å) chelate modes, respectively.

Complex **3** represents a new example of a complex with the $Fe^{III}(\mu$-O)($\mu$-OH)$Fe^{III}$ diamond core.[12−15] The structure of this complex closely resembles that of [(BPEEN)$_2Fe_2^{III}$-($\mu$-O)($\mu$-OH)]$(ClO_4)_3$ [BPEEN = *N*,*N*′-diethyl-*N*,*N*′-bis(2-pyridylmethyl)-ethane-1,2-diamine].[13] In particular, there is a pseudo-$C_2$ axis passing through the O−OH vector, relating both iron centers. The Fe$_2(\mu$-O)($\mu$-OH) core is not disordered owing to hydrogen bonding of the hydroxo bridge proton to a triflate/perchlorate ion, which fixes the position of the proton. The 1.868 Å Fe−$\mu$-O average bond distance is similar to the one reported for the structurally related [(BPEEN)$_2$Fe$_2(\mu$-O)($\mu$-OH)]$(ClO_4)_3$ (1.85 Å)[12,13] and the average Fe−$\mu$-O bond distance observed in [(6-$Me_3$-TPA)$_2$-Fe$_2(\mu$-O)$_2$]$(ClO_4)_2$ (1.88 Å). The 1.994 Å average Fe−$\mu$-OH bond distance compares well with the 1.98 Å of the Fe−$\mu$-

(24) Costas, M.; Que, L., Jr. *Angew. Chem., Int. Ed.* **2002**, *41*, 2179−2181.

OH bond found in $[(BPEEN)_2Fe_2(\mu\text{-}O)(\mu\text{-}OH)](ClO_4)_3$ as well as the 1.99 Å distance determined by EXAFS for $[(6\text{-}Me_3\text{-}TPA)_2Fe_2(\mu\text{-}O)(\mu\text{-}OH)](ClO_4)_3$. The $Fe_2(\mu\text{-}O)(\mu\text{-}OH)$ core of **3** is further characterized by an Fe−O−Fe angle of 100.24(10)° and an Fe−OH−Fe angle of 91.97(9)°, resulting in an Fe−Fe distance of 2.867 Å. This is comparable to that for $[(BPEEN)_2Fe_2(\mu\text{-}O)(\mu\text{-}OH)](ClO_4)_3$ but significantly shorter than the 2.95 Å distance determined by EXAFS for $[(6\text{-}Me_3\text{-}TPA)_2Fe_2(\mu\text{-}O)(\mu\text{-}OH)](ClO_4)_3$.

**Spectroscopic Properties.** Complex **1** exhibits electronic absorption spectra indicative of the presence of a bis($\mu$-hydroxo)diiron(II) core. Its UV−vis spectrum in $CH_2Cl_2$ has an absorption band with $\lambda_{max} = 450$ nm ($\epsilon = 3300$ $M^{-1}$ $cm^{-1}$), which can be assigned to an $Fe^{II}$-to-pyridine charge-transfer transition. Relative to that of the monomeric [(α-BPMCN)$Fe^{II}(CF_3SO_3)_2$], the MLCT band of **1** is red shifted due to the presence of the hydroxide ligands, which diminish the Lewis acidity of the metal center. The $^1$H NMR spectrum of **1** displays 11 relatively sharp well-resolved signals extending from −40 to 120 ppm, a range characteristic of a high-spin $Fe^{II}$ complex. The number of signals and their relative intensities indicate that both Fe sites are equivalent on the $^1$H NMR time scale and that the BPMCN ligand must maintain its $C_2$ symmetric *cis*-α topology in solution. Interestingly, exactly the same $^1$H NMR spectrum is observed for the complex prepared with 1*R*,2*R*-diaminocyclohexane, so there are no additional resonances in the spectrum of the complex derived from racemic diamine that can be ascribed to the *RR*,*SS*-diastereoisomer. While it is still possible for the *RR*,*SS* diastereoisomer to have the same NMR spectrum as the *RR*,*RR*/*SS*,*SS* enantiomeric pairs, it seems highly unlikely given the span of chemical shifts observed. Thus, there appears to be a self-recognition phenomenon at work here that favors formation of only the homochiral dimers of **1**.

Complex **2** exhibits a UV−vis spectrum in $CH_2Cl_2$ with a broad near-IR absorption maximum at $\lambda_{max} = 750$ nm ($\epsilon = 500$ $M^{-1}$ $cm^{-1}$), which accounts for the pale green color of the solution. This band very likely arises from an intervalence charge-transfer transition (a class II complex), as observed for related iron(II)iron(III) complexes.[9,25−27] The $^1$H NMR spectrum of **2** in $CD_2Cl_2$ shows sharp and well resolved signals that extend from −10 to 300 ppm (Figure 2 (middle)); the larger range of shifts compared to that observed for **1** is as expected for a diiron(II,III) complex. Complex **2** exhibits the same number of peaks as **1** with similar relative intensities; thus, electron transfer between iron(II) and iron(III) ions must be fast on the NMR time scale.

The situation is quite different when **2** is dissolved in $CD_3CN$ solution. The $^1$H NMR spectrum reveals the formation of an integer spin $Fe^{II}$(BPMCN) complex, presumably [(α-BPMCN)$Fe^{II}(CD_3CN)_2]^{2+}$, while the EPR spectrum of the same solution, prepared under strictly anaerobic conditions, shows features characteristic of a mononuclear high spin $S = {}^5/_2$ iron center. Thus, **2** appears to dissociate into its corresponding mononuclear components in $CD_3CN$. The features just described are not observed in $CD_2Cl_2$, suggesting that the dinuclear structure of complex **2** is retained in this solvent.

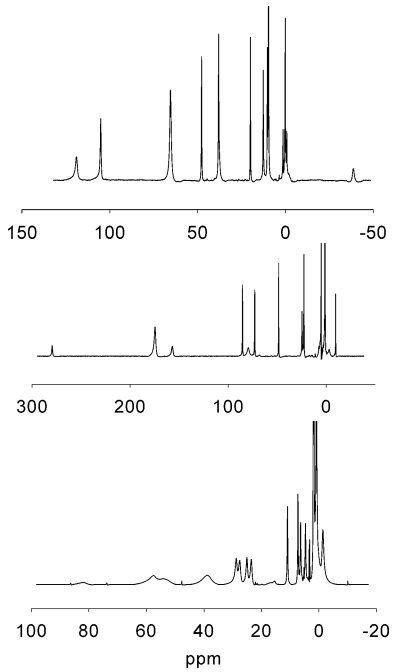


**Figure 2.** Room-temperature 300 MHz $^1$H NMR spectra of **1** (top, $CD_3CN$ solvent), **2** (middle, $CD_2Cl_2$ solvent), and **3** (bottom, $CD_3CN$ solvent). $\delta$-values are listed in Experimental Section.

The spectra of **3** are indicative of the presence of the $Fe^{III}_2(\mu\text{-}O)(\mu\text{-}OH)$ core. Its UV−vis spectrum in $CH_3CN$ displays a visible absorption band with $\lambda_{max} = 558$ nm, $\epsilon = 1600$ $M^{-1}$ $cm^{-1}$, resembling that observed in $[(BPEEN)_2Fe_2(\mu\text{-}O)(\mu\text{-}OH)](ClO_4)_3$[13] and assigned to an oxo-to-iron(III) charge-transfer transition; its relatively low energy compared to those associated with most ($\mu$-oxo)diiron(III) complexes is a consequence of its rather acute Fe−O−Fe angle of 100.24(10)°.[13] The $^1$H NMR spectrum of **3** shows features from 0 to 90 ppm (Figure 2 (bottom)), with broader signals and a more compact range reflecting the moderate antiferromagnetic coupling interaction between the iron(III) ions typical for such cores. For comparison, $[(6\text{-}Me_3\text{-}TPA)_2Fe_2(\mu\text{-}O)(\mu\text{-}OH)](ClO_4)_3$ exhibits signals in the −20 to +80 ppm range and has a $J$ value ($H = J\mathbf{S}_1\cdot\mathbf{S}_2$) of 120 $cm^{-1}$. The number of signals observed for **3**, as well as their relative intensities, further demonstrates that the $C_2$-symmetric *cis*-α topology of the BPMCN ligand is conserved upon oxidation to the diiron(III) state.

**Mössbauer Results. Fe(II)Fe(II) Complex 1.** Figure 3 shows selected variable-temperature spectra of a polycrystalline sample of diferrous complex **1**; data were recorded at 4.2, 30, 60, 100, 140, 160, 200, and 245 K. It can be seen that the spectra consist of two quadrupole doublets, reflecting the structure of **1** in which the two ferrous sites are crystallographically distinct, the actual local site symmetry being $C_1$. At lower temperatures, the doublets are not well

(25) Lee, D.; Krebs, C.; Huynh, B. H.; Hendrich, M. P.; Lippard, S. J. *J. Am. Chem. Soc.* **2000**, *122*, 5000−5001.
(26) Cohen, J. D.; Payne, S.; Hagen, K. S.; Sanders-Loehr, J. *J. Am. Chem. Soc.* **1997**, *119*, 2960−2961.
(27) Hagadorn, J. R.; Que, L., Jr.; Tolman, W. B.; Prisecaru, I.; Münck, E. *J. Am. Chem. Soc.* **1999**, *121*, 9760−9761.

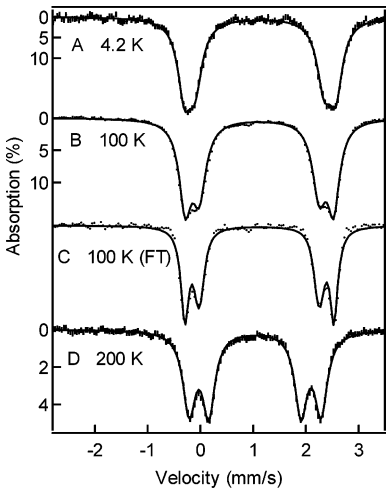


**Figure 3.** Selected zero field Mössbauer spectra of polycrystalline **1** recorded at 4.2 K (A), 100 K (B), and 200 K (D). The spectrum shown in C was obtained from B by removing the line width contribution of the source by a Fourier transform technique. Solid lines in A−D are least-squares fits.

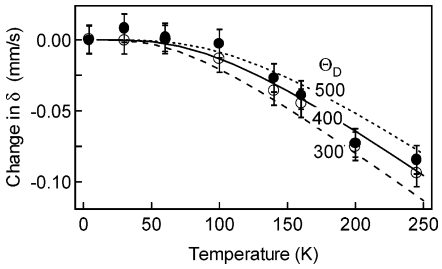


**Figure 4.** Plots of the temperature dependence of $\delta$ for site 1 (●) and site 2 (○) of **1**. The solid line shows the temperature dependence of the second-order Doppler shift in the harmonic approximation for a Debye temperature of 400 K.

resolved; however, this can be improved by applying a Fourier transform technique[28] which effectively removes the line width contribution of the $^{57}$Co(Rh) source. The result of such a deconvolution is shown in Figure 3C.

Figure 4 shows the temperature dependence of the isomer shift for both sites, where the quadrupole splittings and isomer shifts at the indicated temperatures are listed in Table 2. The temperature dependence of $\delta$ reflects the second-order Doppler shift (SOD), which depends in a complicated way on the structure of the solid. In the harmonic approximation, the temperature dependence of SOD can be expressed by the Debye temperature $\Theta_D$[29] using the expression

$$\delta_{SOD} = -\frac{9}{2}\frac{E_0 kT}{mc^2}\left(\frac{T}{\Theta_D}\right)^3 \int_0^{\Theta_D/T} \frac{x^3\,dx}{e^x - 1} \qquad (1)$$

where $E_0 = 14.37$ keV, $m$ is the mass of the $^{57}$Fe nucleus, $k$ is the Boltzmann constant, and $c$ is the speed of light in a vacuum. In Figure 4, we have plotted $\delta_{SOD}$ for three values of $\Theta_D$. A reasonable representation of the experimental data is obtained for $\Theta_D \approx 400$ K.

(28) Dibar-Ure, C.; Flinn, P. A. In *Mössbauer Effect Methodology*; Gruverman, I. J., Ed.; Plenum Press: New York, 1971; Vol. 7, pp 245−262.

(29) Hazony, Y. *Phys. Rev. B* **1973**, *7*, 3309−3314.

**Table 2.** Temperature Dependence of $\Delta E_Q$ and $\delta$ for Diferrous Complex **1** and Mixed-Valence Complex **2′**

| | **1**, site 1 | | **1**, site 2 | | **2′**, $Fe^{II}$ | | **2′**, $Fe^{III}$ | |
|---|---|---|---|---|---|---|---|---|
| temp (K) | $\delta$ (mm/s) | $\Delta E_Q$ (mm/s) | $\delta$ (mm/s) | $\Delta E_Q$ (mm/s) | $\delta$ (mm/s) | $\Delta E_Q$ (mm/s) | $\delta$ (mm/s) | $\Delta E_Q$ (mm/s) |
| 4.2 | 1.12 | 2.45 | 1.13 | 2.87 | | | 0.45 | |
| 18 | | | | | 1.10 | 2.20 | | |
| 30 | 1.12 | 2.47 | 1.13 | 2.91 | 1.10 | 2.14 | | |
| 40 | | | | | 1.06 | 2.17 | | |
| 60 | 1.12 | 2.40 | 1.13 | 2.86 | 1.06 | 2.13 | 0.46 | 0.67 |
| 80 | | | | | 1.06 | 2.08 | 0.47 | 0.67 |
| 100 | 1.12 | 2.27 | 1.12 | 2.82 | 1.04 | 1.93 | 0.48 | 0.65 |
| 140 | 1.09 | 2.10 | 1.10 | 2.74 | 0.97 | 1.80 | 0.49 | 0.60 |
| 160 | 1.08 | 2.01 | 1.09 | 2.71 | | | | |
| 180 | | | | | 0.92 | 1.67 | 0.53 | 0.55 |
| 200 | 1.07 | 1.90 | 1.07 | 2.62 | 0.88 | 1.62 | 0.53 | 0.53 |
| 240 | | | | | 0.85 | 1.55 | 0.57 | 0.53 |
| 245 | 1.03 | 1.74 | 1.04 | 2.48 | | | | |

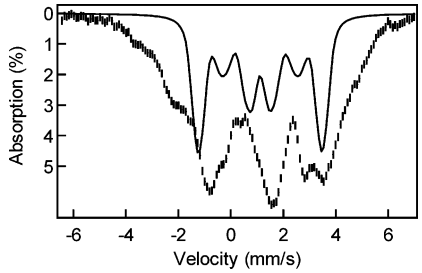


**Figure 5.** The 8.0 T spectrum of **1** recorded at 4.2 K. The solid line is spectral simulation with the (unjustified) assumption that the electronic ground state of the diferrous cluster has $S = 0$ (strong antiferromagnetic coupling).

The temperature dependences of the quadrupole splittings of the two sites of **1** show that both have excited orbital states measurably populated at temperatures above ~30 K. For mononuclear sites, one can generally determine the energies of the low-lying states by fitting the temperature dependence of $\Delta E_Q$ to a crystal field model as described by Ingalls.[30] In the present case this procedure requires knowledge of the exchange coupling constant, $J$, in the orbital ground and excited states due to thermal population of higher spin ladder states which affects the Boltzmann factors entering into the analysis. While a detailed treatment requires knowledge of the energy level scheme of **1**, a rough estimate for the first excited orbital states suggests that they are a few hundred wavenumbers above the ground state.

Figure 5 shows a 4.2 K spectrum of **1** recorded in a field of 8.0 T applied parallel to the $\gamma$-beam. The two iron sites of **1** are likely exchange coupled, but the magnitude and sign of the coupling are not known. For antiferromagnetic coupling with $J \gg D_i$, where the $D_1$ and $D_2$ are the zero-field splitting parameters of the two sites, an $S = 0$ ground state results and the high-field spectrum has a shape characteristic of that observed for a diamagnet. The simulation (solid line) in Figure 5 shows that this assumption is not correct. Rather, the spectral features remind us of a complex with a weak, $|J| < |D_i|$, ferromagnetic coupling, a suggestion supported by the observation of a parallel mode EPR signal at 8 K (recorded in frozen acetonitrile solution; not shown) at $g_{eff} \approx 16$.[11] The high-field spectra of **1** depend

(30) Ingalls, R. *Phys. Rev.* **1964**, *133*, A787−795.

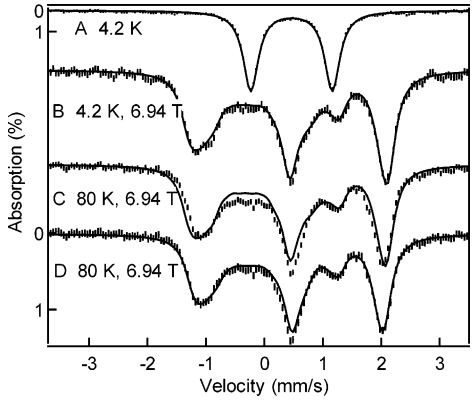


**Figure 6.** Mössbauer spectra of diferric complex **3** recorded at 4.2 K (A, B) and 80 K in applied magnetic fields as indicated. Solid lines are spectral simulations as indicated in the text, using $\Delta E_Q = -1.37$ mm/s, $\eta = 0.1$, and $\delta = 0.46$ mm/s. Experimental data in C and D are identical; the solid line in C was obtained with the assumption that $J = \infty$, while $J = 90$ cm$^{-1}$ was used for the simulation shown in D.

on more than 20 unknowns, and the analysis has not been pursued here.

**Fe(III)Fe(III) Complex 3.** Figure 6 shows Mössbauer spectra of the diferric complex **3** recorded at 4.2 K (A and B) and at 80 K (same data in C and D). Spectrum A was measured in the absence of an applied magnetic field while the spectra of B and C, D were recorded in a parallel field of 6.94 T. The zero-field spectrum consists of a single quadrupole doublet with $\Delta E_Q = 1.37(2)$ mm/s and $\delta = 0.46(1)$ mm/s. The observation of two indistinguishable sites is in accord with the X-ray structure. The solid line in Figure 6B is a spectral simulation based on the assumption that the ground state of **3** is diamagnetic ($S = 0$); moreover, the simulation shows that the assumption is valid, $\Delta E_Q < 0$, and the asymmetry parameter of the electric field gradient tensor has the value $\eta \approx 0$. The observation of a diamagnetic ground state shows that the two iron sites of **3** are antiferromagnetically coupled. In previous work[31,32] we have shown that the exchange coupling constant $J$ ($H = J\mathbf{S}_1\cdot\mathbf{S}_2$) can be determined with Mössbauer spectroscopy provided $J < 120$ cm$^{-1}$. Figure 6C shows a 6.94 T spectrum of **3** recorded at 80 K; the solid line is a spectral simulation generated with the assumption that only the $S = 0$ state is populated at this temperature. It can be seen that the experimental splittings are smaller than predicted by the simulation. The mismatch between theory and data can be attributed to population of the $S = 1$ state of the spin ladder. Under the condition of fast spin relaxation, prevailing here, the reduction of the effective field depends on the $^{57}$Fe magnetic hyperfine coupling constants ($-29 \pm 2$ MHz for this type of ligand environment) and $J$, which controls the Boltzmann factors for averaging the spin expectation values. In effect, $J$ is the only unknown of the 80 K spectrum. By varying $J$, the fit (Figure 6D) reveals $J = +90 \pm 15$ cm$^{-1}$.

**Fe(II)Fe(III) Complex 2′.** The mixed-valence complex has been generated by oxidizing **1** either in air, with [Fe(Cp)$_2$](PF$_6$), or by using solid $AgCF_3SO_3$. Air oxidation has never resulted in preparing a pure sample; however, [Fe(Cp)$_2$](PF$_6$) oxidation produced a sample that was at least 88% pure, with only one minor, spectroscopically known diferric contaminant. Samples oxidized by $AgCF_3SO_3$ had this diferric as well as a diferrous contaminant, and for this reason, we have focused our Mössbauer study on the [Fe(Cp)$_2$](PF$_6$) oxidized sample. In this sample, the mixed-valence complex may contain both triflate and hexafluorophosphate as counterions. In order to distinguish this material from that studied by crystallography (three triflate counterions; **2**), we label the Mössbauer sample as **2′**.

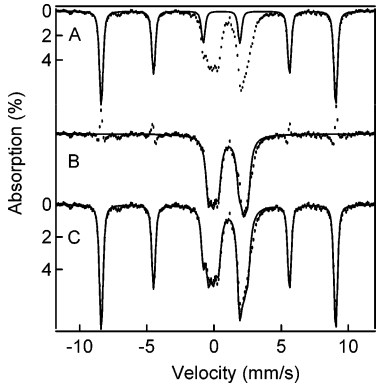


**Figure 7.** Mössbauer spectrum of the mixed-valence complex **2′** recorded at 1.5 K in a parallel field of 0.05 T (A). At this temperature, transitions between the $M_S = -9/2$ and $M_S = +9/2$ states of the $S = 9/2$ multiplet are slow on the Mössbauer time scale, and the spectum is a combination of two distinct sites (Fe$^{III}$ and Fe$^{II}$). The solid line in A is a spectral simulation for the ferric site based on eq 2 using the parameters of Table 3. Spectrum B is the ferrous site contribution obtained after subtraction of the ferric simulation from the original data. The solid line is a spectral simulation for the ferrous site. The sum of the simulations for the ferric and ferrous sites is shown in C along with the original data.

Figures 7−9 and 12−13 show Mössbauer spectra of the mixed-valence complex **2′**. The spectra have a variety of interesting features which we will describe in some detail, starting with the 1.5 K spectrum of Figure 7. Our polycrystalline sample contained an impurity of diferric **3**, accounting for 12% of the iron in the sample. As the spectral features of **3** are well-known over the entire temperature range, we have removed the contribution of this contaminant from all spectra shown. Complex **2′** exhibits distinguishable subspectra for the ferric and ferrous sites and thus belongs to class II (valence-localized) in the Robin−Day classification scheme.[33] At 1.5 K, the spectrum of the Fe$^{III}$ site consists of a simple 6-line pattern, and moreover, the intensities of the absorption lines do not change when the direction of the applied 0.05 T field is changed from parallel to perpendicular with respect to the observed $\gamma$-rays. The resulting spectral patterns are characteristic of a Kramers doublet with anisotropic effective $g$-values $g_z \gg g_x \approx g_y$. For the present mixed-valent system, this information suggests an $S = 9/2$ ground state with a negative zero-field splitting parameter, $D$. Thus, the two irons of **2′** are ferromagnetically coupled. We wish to stress, for what follows, that the electronic spin relaxation process connecting the $M_S = \pm 9/2$ levels of the ground Kramers doublet is slow at 1.5 K; for fast relaxation two

(31) Zang, Y.; Dong, Y.; Que, L., Jr.; Kauffmann, K. E.; Münck, E. *J. Am. Chem. Soc.* **1995**, *117*, 1169−1170.
(32) Kauffmann, K. E.; Münck, E. *ACS Symp. Ser.* **1998**, *692*, 16−29.
(33) Robin, M. B.; Day, P. *Adv. Inorg. Radiochem.* **1967**, *10*, 247−422.

**Table 3.** Fine Structure and Hyperfine Structure Parameters Obtained for Mixed-Valence Complex **2′**[a]

| | $d$[b] ($cm^{-1}$) | $e/d$ | $\Delta E_Q$ (mm/s) | $\eta$ | $(\alpha, \beta, \gamma)_{EFG}$ (deg) | $a_x/g_n\beta_n$ | $a_y/g_n\beta_n$ (T) | $a_z/g_n\beta_n$ | $(0, \beta, \gamma)_A$ (deg) | $\delta$ (mm/s) |
|---|---|---|---|---|---|---|---|---|---|---|
| $Fe^{II}$ | −9 | 0.15 | +2.2 | 1 | −20, 40, −10 | −14[c] | −13[c] | 0.6[d] | −8 | 1.10 |
| $Fe^{III}$ | 0 | 0 | +0.65 | 0.3 | 0, 90, 0 | −21.9 | −21.9 | −21.9 | | 0.45 |

[a] Mössbauer spectra were calculated from eq 4 for $J = -15\ cm^{-1}$. [b] We arbitrarily have set the $d$-value of the ferric site to zero and adjusted the $d$-value of the ferrous site such that $D_{9/2} = -1.5\ cm^{-1}$. [c] $a_x$ and $a_y$ depend on the choice for $(\alpha, \beta, \gamma)_{EFG}$. For $a_{2iso} = (a_{2x} + a_{2y} + a_{2z})/3$, we estimate a range $a_{2iso}/g_n\beta_n = -9.7 \pm 1$ T. [d] Sign unknown.

quadrupole doublets characteristic of a ferric and a ferrous site would result.

We discuss the low-temperature Mössbauer spectra of **2′** within the framework of the $S = {}^9/_2$ Hamiltonian

$$H = \mathbf{S}\cdot\mathbf{D}_{9/2}\cdot\mathbf{S} + \beta\mathbf{S}\cdot\mathbf{g}_{9/2}\cdot\mathbf{B} + \sum_{i=1}^{2}\{\mathbf{S}\cdot\mathbf{A}_i\cdot\mathbf{I}_i - g_n\beta_n\mathbf{B}\cdot\mathbf{I}_i + H_Q(i)\} \quad (2)$$

$$H_Q(i) = \frac{eQV_{i,\zeta\zeta}}{12}[3\mathbf{I}_{i,\zeta}{}^2 - ({}^{15}/_4) + \eta_i(\mathbf{I}_{i,\xi}{}^2 - \mathbf{I}_{i,\eta}{}^2)] \quad (3)$$

where $\mathbf{S} = \mathbf{S}_1 + \mathbf{S}_2$, $D_{9/2}$ and $E$ are the principal values of the zero-field spitting (ZFS) tensor $\mathbf{D}_{9/2}$, $A_1$ is the magnetic hyperfine constant of the ferric ion, $\mathbf{A}_2$ is the **A**-tensor of the ferrous site, and $H_Q(i)$ represents the quadrupole interactions of the two sites, $i = 1, 2$. $(\xi, \eta, \zeta)$ designates the principal axes system of the electric field gradient (EFG) tensor, $\eta_i = (V_{i,\xi\xi} - V_{i,\eta\eta})/V_{i,\zeta\zeta}$ is the asymmetry parameter of site $i$, and $(\alpha, \beta, \gamma)_{EFG}$ and $(\alpha, \beta, \gamma)_A$ are the Euler angles describing the orientation of the EFG tensor and **A**-tensor, respectively, relative to the ZFS tensor (see Table 3). While it is useful to discuss the spectral features by reference to the coupled $S = {}^9/_2$ state, even the low-temperature spectra depend on the exchange coupling constant $J$ ($\approx -15\ cm^{-1}$); the $A$-values obtained from spectral simulations would be in error by ca. 5% if the presence of the $S = {}^7/_2$ multiplet were ignored. Thus, for the final analysis (Table 3) we have computed the Mössbauer spectra by using the uncoupled representation ($S_1 = {}^5/_2$, $S_2 = 2$)

$$H = J\mathbf{S}_1\cdot\mathbf{S}_2 + \sum_{i=1}^{2}\{\mathbf{S}_i\cdot\mathbf{d}_i\cdot\mathbf{S}_i + \beta\mathbf{S}_i\cdot\mathbf{g}_i\cdot\mathbf{B} + \mathbf{S}_i\cdot\mathbf{a}_i\cdot\mathbf{I}_i - g_n\beta_n\mathbf{B}\cdot\mathbf{I}_i + H_Q(i)\} \quad (4)$$

For the $S = {}^9/_2$ multiplet, the parameters of the coupled representation (capital letters) are related to those of the uncoupled representation (low case) by $A_1 = ({}^5/_9)a_1$, $\mathbf{A}_2 = ({}^4/_9)\mathbf{a}_2$, $\mathbf{g}_{9/2} = ({}^5/_9)g_1 + ({}^4/_9)\mathbf{g}_2$, and $\mathbf{D}_{9/2} = + ({}^5/_{18})\mathbf{d}_1 + ({}^1/_6)\mathbf{d}_2$, for $|J| \gg |d_1|, |d_2|$. Throughout this manuscript we assume that $\mathbf{d}_1$ and $\mathbf{d}_2$ are collinear; hence all Euler angles refer to the principal axis system of $\mathbf{D}_{9/2}$. In fact, since essentially only $\mathbf{D}_{9/2}$ matters for the analysis, we have set $\mathbf{d}_1 = 0$ (see footnote in Table 3).

Figures S1 and S2 show EPR spectra of polycrystalline **2** recorded at 2.3, 6.6, 9.6, and 12.9 K. The spectra exhibit broad features which, to a large extent, can be attributed to substantial spin−spin interactions of neighboring molecules in the solid. (There are four molecules in the unit cell, with center−center distance ranging from 9.8 to 16 Å.) We have at best a qualitative understanding of the spectra, but we are reasonably certain that the features centered around $g = 7.5$ and $g = 2.8$ belong to different excited Kramers doublets of the $S = {}^9/_2$ multiplet. The EPR spectra depend on the intrinsic $g$-values of the ferrous site (which may substantially deviate from $g = 2.0$; see below), the rhombicity parameter $E/D$, and moreover, some of the resonances depend also on $J$ (through mixing of the $S = {}^9/_2$ and ${}^7/_2$ multiplets by the ZFS terms). Roughly, the EPR data suggest $E/D \approx 0.15$ (see Supporting Information) and the Mössbauer spectra of solid **2′** are compatible with this value.

The Mössbauer spectrum of the $Fe^{III}$ site, accounting for 50% of the absorption in Figure 7, belongs to the $M_S = \pm{}^9/_2$ doublet and is well simulated for $D < 0$, $a_1/g_n\beta_n = -21.9$ T, $\Delta E_Q = +0.65$ mm/s, $\eta = 0.3$, $\beta_{EFG} = 90°$, and $\delta = 0.45$ mm/s. Owing to the magnetic anisotropy of the $M_S = \pm{}^9/_2$ state, the 1.5 K spectrum is sensitive only to the $z$-component of the EFG tensor, but since $\Delta E_Q$ is known from the high-temperature data of Figure 12, the asymmetry parameter $\eta$ can be determined from the 1.5 K spectrum. Our analysis shows that the largest component of the EFG tensor is perpendicular, $\beta_{EFG} = 90°$, to the $z$-axis of the ZFS tensor.

The $Fe^{II}$ site exhibits very small magnetic splittings at 1.5 K, corresponding to $|A_{2z}/g_n\beta_n| \approx 0.4$ T. The small value of $A_{2z}$ can be rationalized by observing that the **A**-tensors of high-spin ferrous sites have substantial anisotropies and assuming that the easy axis of magnetization, the $z$-axis of the ZFS tensor, is (nearly) along the smallest component of $\mathbf{A}_2$.

Figure 8A shows an 8.0 T spectrum recorded at 4.2 K. From these data, we can determine $D_{9/2}$ and the remaining hyperfine parameters of the ferrous site. Above Figure 8A we have plotted a theoretical spectrum for the $Fe^{III}$ site, based on the parameters obtained in low field, and assuming $D_{9/2} = -20\ cm^{-1}$. It can be seen that the computed absorption lines are too broad, which can be understood as follows. For a large $D_{9/2}$, the $M_S = \pm{}^9/_2$ doublet is well isolated from the other sublevels of the $S = {}^9/_2$ multiplet, and consequently, the expectation values of the electronic spin is fixed along the $z$-axis of the ZFS tensor, $\langle S_z\rangle = -{}^9/_2$. For the $M_S = -{}^9/_2$ state the applied field, **B**, opposes the fixed internal field, $\mathbf{B}_{int} = -54.2$ T, in a way that depends on the direction of **B** relative to the molecular $z$-axis. This leads, for a polycrystalline sample, to a distribution of the effective magnetic field at the nucleus, $\mathbf{B}_{eff} = \mathbf{B}_{int} + \mathbf{B}$, and therefore to a broadening of the absorption lines. As the magnitude of $D_{9/2}$ is reduced, mixing of the $M_S = -{}^9/_2$ state with the $M_S = -{}^7/_2$ level produces a sizable magnetization in the $x-y$ plane, e.g., $\langle S_x\rangle = \langle S_y\rangle = -3.16$ for $D_{9/2} = -1.5\ cm^{-1}$

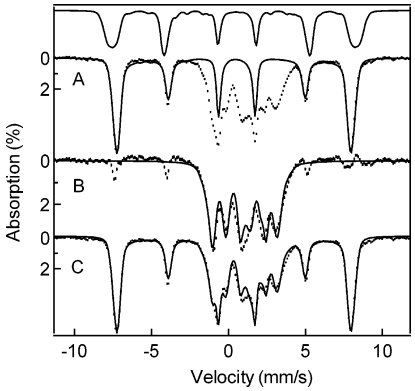


**Figure 8.** The 4.2 K spectrum of **2′** recorded in a magnetic field of 8.0 T applied parallel to the $\gamma$-beam (A). The solid line drawn above A represents a simulation for the $Fe^{III}$ spectrum assuming a very large $D_{9/2}$-value. The solid line in A was obtained with the parameters of Table 3 for $D_{9/2} = -1.5\ cm^{-1}$. The spectrum in B, representing the ferrous site, was obtained by subtracting the simulation of the $Fe^{III}$ site from the data of A. The solid line in B is a simulation using the parameters listed in Table 3. C again shows the raw data (minus the diferric contaminant described in the text) together with the simulation for both sites (sum of the solid lines in A and B).

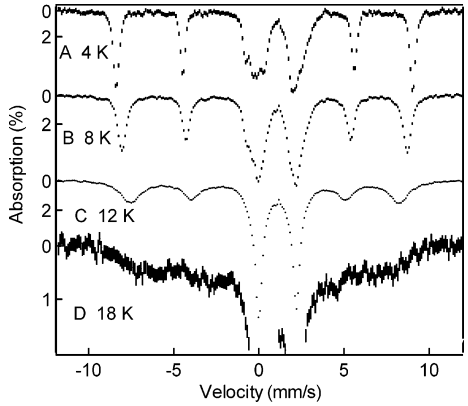


**Figure 9.** Variable-temperature Mössbauer spectra of **2′** recorded in parallel 0.05 T applied fields at the temperatures indicated. At 18 K the spectrum of the ferric site is spread over a velocity of 15 mm/s, while that of the ferrous site (center) has collapsed into a quadrupole doublet; for clarity the contribution of the ferric site is shown enlarged in (D), with the absorption of the ferrous site truncated.

and $B = 8.0$ T. The induced $x-y$ magnetization tilts $\mathbf{B}_{int}$ away from the $z$-axis toward the applied field, resulting in a narrower distribution for $\mathbf{B}_{eff}$, and thus sharper absorption features. Hence, the line shapes convey information about $D_{9/2}$. The solid line drawn through the data of Figure 8A was obtained for $D_{9/2} = -1.5\ cm^{-1}$. We show below that we obtain independently the same value for $D_{9/2}$ by considering the temperature dependence of $\mathbf{B}_{int}$.

The spectrum in Figure 8B, representing the $Fe^{II}$ site of **2**, was obtained by subtracting the simulated spectrum of the $Fe^{III}$ site from the data of Figure 8A. We showed above that $|A_z/g_n\beta_n| \approx 0.4$ T for the ferrous site. Because the isotropic part of the $\mathbf{a}_2$-tensor of a six-coordinate $Fe^{II}$ site yields typically (at saturation) a $\mathbf{B}_{int}$ between $-16$ and $-20$ T, it follows that the $x$- and $y$-components of $\mathbf{A}_2$ must be substantially larger than $A_{2z}$. This suggests that the magnetic splittings of the spectrum of Figure 8B are dominated by $A_{2x}$ and $A_{2y}$ (because $<S_x>A_{2x}$ and $<S_y>A_{2y}$ are large). Since the $x$- and $y$-components of $\mathbf{A}_2$ are substantially larger than $A_{2z}$, the latter must be nearly aligned with the $z$-axis of the ZFS tensor; otherwise, the 0.05 T spectrum of the $Fe^{II}$ site would exhibit larger splittings. Spectral simulations suggest that the principal direction $A_{2z}$ must coincide within 10° with the $z$-axis of the ZFS tensor (with the final fit settling at ca. 8°). The ferrous EFG tensor does not necessarily have the same principal axis system as $\mathbf{A}_2$. In fact, all simulations that produced the 8.0 T spectrum of Figure 8B reasonably well required that the EFG-tensor is rotated relative to the ZFS tensor and $\mathbf{A}_2$. For the ferrous site, we are thus left with the determination of seven unknowns, namely, in the language of eq 4, $a_{2x}$, $a_{2y}$, sign $\Delta E_Q(2)$, the asymmetry parameter $\eta_2$, and the Euler angles that relate the EFG tensor to the frame of the ZFS tensor. Some of the parameters are highly correlated, and thus, similar simulations resulted for different parameters sets. However, the following features emerged from the simulations: The sum of $a_{2x}/g_n\beta_n$ and $a_{2y}/g_n\beta_n$ is ca. $-28$ T, and $\beta_{EFG}$ is ca. 30−60°. Moreover, the asymmetry parameter of the EFG tensor is close to $\eta_2 = 1$, as suggested by the symmetry of the 8.0 T spectrum. The solid line in Figure 8B is a simulation for the ferrous site of **2′**; for this simulation we have used the parameters listed in Table 3. (The choice for the exchange coupling constant will be addressed after a discussion of Figure 12.)

Figure 9 shows 0.05 T spectra of **2′** recorded at 4.2, 8, 12, and 18 K. It can be seen that the magnetic splitting of the nuclear levels of the $Fe^{III}$ site decreases with increasing temperature. This decrease is accompanied by a broadening of the absorption lines. At 18 K the spectrum of the ferric site is featureless and spreads over a velocity range of 15 mm/s. The broad distribution of absorption at 18 K is characteristic of paramagnetic relaxation,[34] and this observation thus argues against the possibility that polycrystalline **2′** is a solid exhibiting long-range order. The continuous decrease of the internal magnetic field, $\mathbf{B}_{int}(Fe^{III})$, between 1.5 and 12 K demonstrates fast relaxation of the electronic spin between the equally signed $M_S$ sublevels of the $S = {}^9/_2$ manifold. Specifically, the experimental data suggest the situation depicted in Figure 10. Thus, thermally activated Orbach processes allow fast $\Delta M_S = \pm 1$ transitions, and the system can cascade up and down the ladders consisting of levels with either positive or negative $M_S$ values; expressions for such phonon-assisted relaxation rates have been given by Leuenberger and Loss.[35] For $E/D < 0.05$, crossing between the two halves of the ladder, along the path labeled $k_x$, occurs essentially in the $M_S = \pm {}^1/_2$ doublet; the other $M_S$ sign-flipping crossings, the ones generally referred to as spin tunneling, are strongly inhibited though not strictly forbidden (see ref 35). For $T \leq 12$ K we are thus dealing with a system that can be described by two effective relaxation rates: The vertical processes (double arrows) are fast even at 4.2 K, while relaxation along the horizontal path is slow at $T \leq$ 4.2 K, primarily because the $M_S = \pm {}^1/_2$ levels are not populated (see qualifying comment in figure caption). Since the relaxation along the vertical scale in Figure 10 is fast,

(34) Wickman, H. H.; Klein, M. P.; Shirley, D. A. **1966**, *152*, 345−357.
(35) Leuenberger, M. N.; Loss, D. *Phys. Rev. B* **2000**, *61*, 1286−1302.

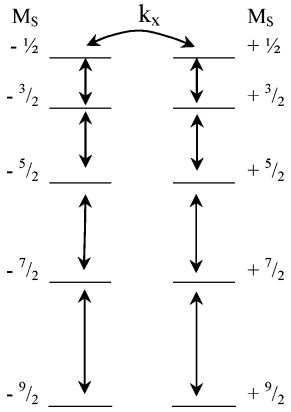


**Figure 10.** Main relaxation pathways within the $S = {}^9/_2$ multiplet. Relaxation rates along vertical paths are assumed to be fast on the time scale of Mössbauer spectroscopy (here ca. 30 MHz). For $E/D \approx 0.15$ as assumed in the text, the $M_S = \pm{}^3/_2$ and $\pm{}^5/_2$ levels acquire substantial $\pm{}^1/_2$ admixtures, and the $k_x$ processes will therefore involve at least three doublets.

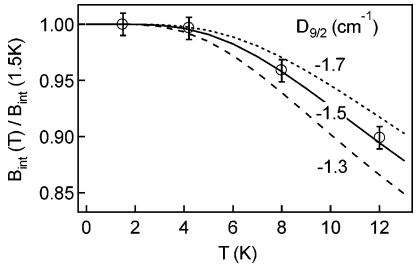


**Figure 11.** Plot of $B_{int}$ versus temperature for polycrystalline complex **2′**. The solid line is a fit to eq 5 for $D_{9/2} = -1.5$ cm$^{-1}$.

the $^{57}$Fe nucleus of the ferric site senses a hyperfine field corresponding to $\mathbf{B}_{int} = -A_1 \langle S_z \rangle_{th} / g_n \beta_n$, where $\langle S_z \rangle_{th}$ is the thermally averaged spin; the sign of $\mathbf{B}_{int}$ is negative when the average is performed for the levels with negative $M_S$-values ($A_1 < 0$ for Fe$^{III}$). In the absence of an applied field, the right and left levels of Figure 10 yield identical Mössbauer spectra. Relaxation between the left and right sides of this $M_s$-ladder leads to a reversal of the hyperfine field with a rate primarily determined by $k_x$. For slow $k_x$ processes, the Mössbauer spectrum consists of a 6-line pattern with sharp lines; however, as relaxation through the $k_x$ pathway(s) increases, the absorption lines broaden, and the magnetically split pattern finally collapses, at around $T = 60$ K, into a quadrupole doublet with $\Delta E_Q = 0.67$ mm/s and $\delta = 0.46$ mm/s. We have analyzed the temperature dependence of the internal field by assuming that the population in each ladder of the $S = {}^9/_2$ multiplet follows a Boltzmann distribution

$$\mathbf{B}_{int}(T) = \frac{-A_1}{g_n \beta_n} \frac{\sum_{M_S} M_S e^{-D_{9/2} M_S^2 / kT}}{\sum_{M_S} e^{-D_{9/2} M_S^2 / kT}} \qquad (5)$$

The temperature dependence of $\mathbf{B}_{int}$(Fe$^{III}$) is well fitted for $D_{9/2} = -1.5 \pm 0.1$ cm$^{-1}$; see Figure 11 (using $E/D = 0.15$ instead of $E/D = 0$ yields $D_{9/2} = -1.55$ cm$^{-1}$). It should be noted that we have obtained the same value for $D_{9/2}$ by two

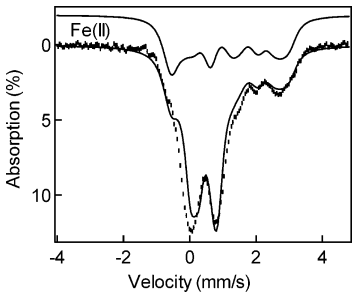


**Figure 12.** The 8.0 T Mössbauer spectrum of **2′** recorded at 100 K. The solid line drawn through the data is a spectral simulation, based on eq 4, for $J = -15$ cm$^{-1}$ assuming fast relaxation among all thermally accessible levels and using the parameters listed in Table 3. The Fe$^{II}$ contribution is indicated separately above data.

independent methods. This method yields $D_{9/2}$ by fitting a Boltzmann distribution to the sublevels of the $S = {}^9/_2$ multiplet in weak (or zero) applied field, while the other determines $D_{9/2}$ by the degree of mixing between $M_S$ sublevels in a strong applied field. Considering that *d*-values for ferrous and ferric sites with octahedral N/O coordination are typically 4−10 and 1−2 cm$^{-1}$, respectively, the result for $D_{9/2}$ is reasonable; recall $\mathbf{D}_{9/2} = ({}^1/_6)\mathbf{d}_2 + ({}^5/_{18})\mathbf{d}_1$.

Figure 12 shows an 8.0 T spectrum recorded at 100 K, a temperature at which the electronic system is in the fast fluctuation limit (in small applied fields). Since the hyperfine parameters of the ferric site and the zero-field splitting parameters of the $S = {}^9/_2$ multiplet are known from the analysis of the low-temperature spectra, the 100 K high-field spectrum of the ferric site can be calculated provided that only the $S = {}^9/_2$ multiplet of the spin ladder is populated at 100 K. Such a calculation revealed that the magnetic splittings of both sites are ca. 10% too large, suggesting that the $S = {}^7/_2$ multiplet must be measurably populated at 100 K. This observation provides a means to estimate the exchange coupling constant *J*. Spectral simulations for the ferric site strongly suggest that $|J| < 25$ cm$^{-1}$; for larger *J*-values the spectrum of the ferric site develops a triplet structure not observed experimentally. (The solid line plotted above the data is a simulation for the ferrous site; the central doublet-type structure is the contribution of the ferric site.) Although all spin Hamiltonian parameters, except *J*, are known, the simulations for the ferric site are not satisfactory; in particular, the simulation seems to miss the low energy feature. Various possibilities have been considered for the ferric site to obtain better simulations, including rotation of the **d**-tensors of the ferric (for $\mathbf{d}_1 \neq 0$) and ferrous sites. However, none of these attempts produced a satisfactory simulation for the low energy feature of the ferric site. Perhaps our assumption of fast relaxation, while correct in weak applied fields, does not strictly apply at 8.0 T. It is conceivable that some sublevels of the exchange coupled system are not connected with the other sublevels by fast relaxing pathways. (Note that the $M_S = \pm{}^9/_2$ levels, for instance, have a Zeeman splitting of ca. 70 cm$^{-1}$ for $B_z = 8$ T, and thus, the level scheme is substantially altered in high field.)

Figure 13 shows selected high-temperature spectra of **2′**. Above 80 K, the spectra of **2′** consist of two quadrupole

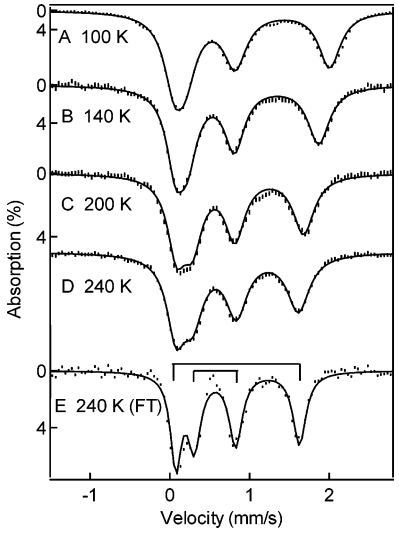


**Figure 13.** High-temperature Mössbauer spectra of polycrystalline **2′**. Spectrum E after Fourier transform treatment of D. The nested assignment of the doublets is indicated by the brackets.

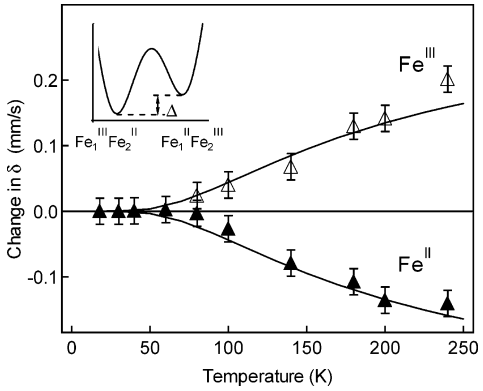


**Figure 14.** Temperature dependence of the isomer shifts after correction for SOD. Errors were estimated from spectral simulations of the spectra in Figure 13. The solid lines are a fit to a two-state model for $\Delta = 180$ cm$^{-1}$. The insert is a cartoon depicting thermal activation for a two-state process.

doublets. The isomer shifts of both iron sites, after correction for SOD, were found to be temperature dependent in a pattern suggesting increased electron hopping as the temperature increases. In order to increase the resolution of the spectra, we have removed the line width contribution of the $^{57}$Co(Rh) source from all spectra using the aforementioned Fourier transform procedure. Figure 13D shows a 240 K spectrum of **2′**, and Figure 13E shows the same spectrum after removal of the source line width. Despite the added precision due to the transform procedure, the data allow two possible assignments for the four absorption lines of the quadrupole doublets, namely a nested pair of lines (brackets in Figure 13E) and a non-nested association of the lines. For instance, at 80 K we obtained (in mm/s) $\Delta E_Q(Fe^{III}) = 0.67$, $\delta(Fe^{III}) = 0.47$, $\Delta E_Q(Fe^{II}) = 2.08$, $\delta(Fe^{II}) = 1.06$ for the nested assignment, and $\Delta E_Q(Fe^{III}) = 0.78$, $\delta(Fe^{III}) = 0.41$, $\Delta E_Q(Fe^{III}) = 1.97$, $\delta(Fe^{III}) = 1.11$ for the alternative assignment. This ambiguity can be resolved by making use of the fact that the spectrum of the ferrous site depends little on the temperature between 30 and 80 K (not shown), while the spectrum of the ferric site is broad and unresolved at 30 K due to paramagnetic relaxation, but quite sharp at 80 K. The difference spectrum (80 K minus 30 K) displays essentially one well-defined doublet with $\Delta E_Q = 0.67(3)$ mm/s and $\delta = 0.47(2)$ mm/s for the ferric site at 80 K. Thus, the nested pairing (Table 2) is the correct assignment. After correction for SOD, using the results from **1**, we obtain the isomer shifts plotted in Figure 14. The corrected $\delta(Fe^{II})$ decreases uniformly above 100 K while $\delta(Fe^{III})$ increases, suggesting that the ferric site acquires ferrous character while the ferric site becomes more ferrous.

We do not yet know the details of the electron hopping mechanism, such as the rate, how many electronic states are involved, etc. In Figure 14 we consider a simple 2-state mode involving the electronic configurations $Fe_1^{III}Fe_2^{II}$ and $Fe_1^{II}Fe_2^{III}$ separated by energy $\Delta$. Thermally activated transitions between the two states, which are fast compared to the nuclear precession time, result in isomer shifts that are the population-weighted averages of the shifts in these states. The averaged isomer shifts obtained at sites 1 and 2 for $\Delta = 180$ cm$^{-1}$ are presented by the solid lines drawn through the data of Figure 14.

Finally, we have recorded some Mössbauer spectra of the closely related mixed-valence complex $[(BPMEN)_2Fe^{II}Fe^{III}(\mu\text{-}OH)_2](CF_3SO_3)_3$ (**4**). The 4.2 K, 0.05 T, Mössbauer spectrum of this complex is essentially identical to that shown in Figure 7A; in the language of eq 2, $\Delta E_Q = 0.71$ mm/s, $\delta = 0.45$ mm/s, and $A_1 = -12.0$ T for the ferric site and $\Delta E_Q = 2.22$ mm/s, $\delta = 1.10$ mm/s, and $A_{2z} = -0.5$ T for the ferrous site. However, there is no indication of electron hopping for temperatures below 240 K, as witnessed by the observation that the temperature dependence of $\delta$ is entirely accounted for by the second-order Doppler shift.

## Discussion

Our studies of the mixed-valence complex **2′** have yielded a variety of interesting results. Thus, **2′** exhibits ferromagnetic coupling with $J \approx -15$ cm$^{-1}$ ($H = J\mathbf{S}_1\cdot\mathbf{S}_2$), yielding an $S = {}^9/_2$ ground state. The $J$-value was obtained from the analysis of the 8.0 T spectrum recorded at 100 K (Figure 12). As pointed out in the Results section, there are some spectral features of the ferric site in the 100 K spectrum which we were not quite able to simulate. Since the simulation of the Mössbauer spectra for the ferric site yields $J$, this parameter may have an uncertainty of $\pm 5$ cm$^{-1}$. The energy separation between the $S = {}^9/_2$ and $S = {}^7/_2$ multiplets is nearly 70 cm$^{-1}$. For a separation of this magnitude, mixing of the multiplets by the zero-field splitting terms of eq 4 cannot be ignored. For this reason the Mössbauer spectra of Figures 7−9 and 12 have been analyzed using the uncoupled representation of eq 4, although the essential features of the spectra are reasonably well described by consideration of only the ground multiplet.

The $S = {}^9/_2$ ground multiplet of **2′** has uncommon relaxation properties at temperatures below 20 K. Judging from the sharp lines exhibited by the ferric site at temperatures ≤12 K, the interconversion between the $M_S = +{}^9/_2$ and $-{}^9/_2$ members of the ground multiplet is slower than $\approx 10^6$ s$^{-1}$. Fast relaxation processes ($> 10^8$ s$^{-1}$) begin to have

an effect in the range 4.2 K $\leq T \leq$ 12 K in the form of the vertical cascading processes depicted in Figure 10. For simplicity, let us assume that there are only $M_S - M_S' = \pm 1$ transitions. In this case we can distinguish between $M_S \leftrightarrow M_S'$ transitions for which $M_S$ and $M_S'$ have equal signs and those that alter the sign, namely $^1/_2 \leftrightarrow -^1/_2$ (the only transition for $E/D \approx 0$). The Mössbauer spectra can be assigned to roughly three temperature regimes: $T < 4.2$ K, where there is only significant population of the $\pm^9/_2$ levels, leading to spectra with sharp lines and maximum magnetic splitting. 4.2 $\leq T \leq$ 12 K, for which there is significant population of the levels with $|M_S| < {}^9/_2$. In the latter regime, all allowed transitions are fast, but the total number of sign-changing transitions per unit of time is small because the population of the $M_S = \pm^1/_2$ levels is low, resulting in spectra with sharp but inwardly displaced lines. And $T > 12$ K, where the number of sign changes of $M_S$ per unit time becomes large due to the increased thermal population of the $M_S = \pm^1/_2$ levels, leading to a collapse of the magnetic spectra. Fast processes may occur when the ground state acquires considerable unquenched orbital angular momentum, such as that obtained through spin−orbit coupling at the ferrous site in **2′**. (The large magnitude of $d_2 = -9$ cm$^{-1}$ implies that the ground state has considerable orbital angular momentum.) The unusual relaxation properties of **2′** have allowed us to measure the zero-field splitting, $D_{9/2}$, of the ground multiplet with good precision, obtaining $D_{9/2} = -1.5 \pm 0.1$ cm$^{-1}$, in accordance with the result for this quantity inferred from the field dependence of the line widths.

In the Results section, we used $d_2 = -9$ cm$^{-1}$ and $d_1 = 0$ for the zero-field splitting parameters of the ferrous and ferric sites, respectively. Although these parameters cannot be unambiguously determined from the value measured for net zero-field splitting parameter, $\mathbf{D}_{9/2} = (^5/_{18})\mathbf{d}_1 + (^1/_6)\mathbf{d}_2$, the predominance of the $d_2$ term is supported by data for mononuclear sites. Studies of six-coordinate complexes with N/O coordination have shown that $|d_1| \approx 1$ cm$^{-1}$. Using $|d_1| = 1$ cm$^{-1}$ and $D_{9/2} = -1.5$ cm$^{-1}$, we estimate that $d_2 = -9 \pm 2$ cm$^{-1}$. This value is not unreasonable as can be seen by considering the magnetic hyperfine interactions of the ferrous site. The $\mathbf{a}_2$ tensor has three contributions, $\mathbf{a}_2 = a_c + \mathbf{a}_{s-d} + \mathbf{a}_L$. For octahedral $FeN_4O_2$, the isotropic Fermi contact term, $a_c = \kappa P$ ($\kappa = -0.35$, $P = 2\beta\beta_n\langle r^{-1}\rangle \approx 60$ T),[11] is expected to be $a_c/g_n\beta_n \approx -21$ T. The spin-dipolar contribution to $\mathbf{a}_2$, $\mathbf{a}_{s-d}$, is traceless and does not contribute to $a_{2iso} = (a_{2x} + a_{2y} + a_{2z})/3$. In the spin Hamiltonian approximation[36] the orbital contribution is given by $\mathbf{a}_L = (\mathbf{g}_2 - 2)P$ where $\mathbf{g}_2$ is the **g**-tensor of the ferrous site. $\mathbf{a}_L$ can be decomposed into an isotropic ($a_{pc}$, pseudocontact term) and an anisotropic contribution; the latter does not contribute to $a_{2iso}$. For **2′** we take from Table 3 (see footnote of the table) $a_{2iso}/g_n\beta_n \approx -9.7$ T and obtain for the pseudocontact term $a_{pc}/g_n\beta_n = (g_{2iso} - 2)P = a_{2iso}/g_n\beta_n - a_c/g_n\beta_n = -9.7$ T $+21$ T $= +11.3$ T. From these expressions we estimate $g_{2iso} = (g_{2x} + g_{2y} + g_{2z})/3 = 2.19$. In the case of a six-coordinate high-spin ferrous ion, $\mathbf{g}_2$ and $\mathbf{d}_2$ are related by an expression given in ref 37. This relationship can be used to estimate $\mathbf{d}_2$. Since we do not know the precise value of the rhombicity parameter, we consider the case of axial symmetry, $g_{2x} = g_{2y} = 2.28 = g_{2z} - 2d_2/\lambda$, using the spin−orbit coupling constant $\lambda \approx -80$ cm$^{-1}$ and $g_{2z} \approx 2.0$. For $g_{2iso} = 2.19$, this yields $d_2 \approx -11$ cm$^{-1}$, in reasonable agreement with our result. A large value of $d_2$ is also supported by the temperature dependence of $\Delta E_Q(2)$, which indicates the presence of a low-lying orbital excited state at an approximate energy of 300 cm$^{-1}$.

Our analysis shows that the symmetry at the ferrous site is rather low, probably $C_1$, as witnessed by the observation (Table 3) that the principal axes of the EFG and $a_2$-tensors are rotated relative to each other. The low symmetry of **2′** and the presence of low-lying orbital states prevent us presently from exploring the electronic structure of the mixed-valence state with density functional theory calculations. (Geometry optimizations of **2** would take months on our PCs.)

Earlier we have reported the observation of electron hopping in a $[2Fe-2S]^{1+}$ cluster of a 2Fe ferredoxin and in the synthetic complex $[Fe_2(salmp)_2]^{1-}$; (salmp = bis-(salicyledeneamino)-2-methylphenolate(3−)).[38−40] These studies have shown that the hopping rate and mechanism depend on conformational substates of the ferredoxin and on the microenvironment of the $[Fe_2(salmp)_2]^{1-}$ complex; for the latter the hopping rates were observed to be different in frozen solution and crystalline powders, and they depended on the number and type of solvate molecules. The phenolate-bridged $[Fe_2(salmp)_2]^{1-}$ is of interest for the present discussion in that its Fe−Fe distance (3.10 Å at 293 K) is very similar to that in **2** (3.02 Å at 173 K). Moreover, $[Fe_2(salmp)_2]^{1-}$ is ferromagnetically coupled and exhibits the same $J$-value ($-17$ cm$^{-1}$) as complex **2′**. For $[Fe_2(salmp)_2]^{1-}$, electron hopping is observed between ≈100 and 300 K, and the process depends on the physical state of the sample in a rather complex way. The hopping rate in $[Fe_2(salmp)_2]^{1-}$ approaches the precession frequency of the $^{57}$Fe nuclei, resulting in complex line shapes that could only be analyzed by using stochastic line shape theory. In contrast, the hopping in polycrystalline **2′** is fast on the Mössbauer time scale (≈$10^7$ s$^{-1}$) at temperatures where there is evidence of this phenomenon.

Figure 14 shows a fit of the SOD-corrected isomer shifts of the ferric and ferrous sites to a two-state model with energy splitting $\Delta \approx 180$ cm$^{-1}$. The system is trapped in the $Fe_1^{III}Fe_2^{II}$ ground state below 100 K. Above this temperature there is also a sizable probability to find the extra electron at site 1, resulting in the configuration $Fe_1^{II}Fe_2^{III}$. This description, of course, is rather simplified. It ignores

(36) *Electron Paramagnetic Resonance of Transition Ions*; Abragam, A., Bleaney, B., Eds.; New York: Oxford University Press, 1986.

(37) Zimmermann, R.; Spiering, H.; Ritter, G. *Chem. Phys.* **1974**, *4*, 133−141.

(38) Achim, C.; Bominaar, E. L.; Staples, R. J.; Münck, E.; Holm, R. H. *Inorg. Chem.* **2001**, *40*, 4389−4403.

(39) Achim, C.; Bominaar, E. L.; Meyer, J.; Peterson, J.; Münck, E. *J. Am. Chem. Soc.* **1999**, *121*, 3704−3714.

(40) Meyer, J.; Gagnon, J.; Gaillard, J.; Lutz, M.; Achim, C.; Münck, E.; Petillot, Y.; Colangelo, C. M.; Scott, R. A. *Biochemistry* **1997**, *36*, 13374−13380.

that upon each orbital manifold a spin ladder is built, reflecting the ferromagnetic coupling. Moreover, the ferrous site in $Fe_1^{III}Fe_2^{II}$ is in fast equilibrium with low-lying orbital excited states of $Fe_2^{II}$, as can be concluded from the strong temperature dependence of $\Delta E_Q$ of the ferrous site. (The data of Figure 3 and Table 2 show the presence of low-lying orbital states in diferrous **1** as well.) Given the large number of unknowns and the many states involved, a calculation of the effects of electron hopping on the EFG tensors will inevitably raise the concern of overparametrization and has not been attempted. The electron hopping is also apparent from the temperature dependence of $\Delta E_Q$ at the ferric site. Since excited quartet states of high-spin ferric ions are thermally inaccessible, the quadrupole splitting is generally independent of temperature. However, as can be seen from inspection of Table 2, $\Delta E_Q$ of the ferric site of **2′** changes noticeably with temperature, undoubtedly as a consequence of electron hopping.

The delocalization process described for **2′** occurs by thermally activated hopping of the "extra" electron in $d^6$. This phenomenon is quite different from valence-delocalization that accompanies double exchange interactions. The latter are observed for some mixed-valence dimers with Fe−Fe distances shorter than ≈ 2.8 Å.[25,41,42] Hagadorn and co-workers[27] have described a complex where a conformational change of two bridging isopropoxides switches the complex from valence-delocalized (Fe−Fe = 2.62 Å) to valence-trapped (Fe−Fe = 2.71 Å). At longer Fe−Fe distances, 3.03 Å for complex **2**, the mixed-valence state exhibits localized $Fe^{III}$ and $Fe^{II}$ states, and hopping may occur at higher temperature by thermal activation over a barrier, as in $[Fe_2(salmp)_2]^{1-}$ and **2′**.

How do the Mössbauer data of polycrystalline **2′** relate to the X-ray structure of Figure 1? According to the X-ray structure of **2**, taken at 173 K, this complex is class II valence-localized, and we would expect to observe at 173 K Mössbauer spectra with negligible electron hopping. Like **2**, **2′** is also class II valence-localized, but because of electron hopping the Mössbauer spectra exhibit the onset of averaging between the sites. Hopping in class II valence-localized complexes is affected by very subtle differences in the molecular environment and small changes in the molecular conformation.[43] Subtleties that may control electron hopping can be appreciated with reference to the aforementioned $[Fe_2(salmp)_2]^{1-}$ complex, for which electron hopping depends sensitively on the physical state of the sample.[38] Thus, while all $[Fe_2(salmp)_2]^{1-}$ samples studied had identical (and highly resolved) spectra at 4.2 K (see Figure 2 of ref 38), the samples differed markedly in the temperature regime between 100 and 250 K. For instance, crystals containing MeCN solvate molecules were valence-localized at all temperatures while those containing two DMF solvate molecules exhibited a collapse into a valence-averaged spectral component above 100 K due to electron hopping, and crystals with partially depleted solvate showed various patterns of dynamical behavior. We have also obtained a crystal structure of the mixed-valence complex (not shown) by oxidizing **1** in air; this structure was found to have disordered $Fe_2(OH)_2$ cores such that the apparent Fe−O distances for the two sites were quite similar. A disordered structure was also reported by Egdal et al.[9] for $[(BPMEN)_2Fe^{II}Fe^{III}(\mu\text{-}OH)_2](ClO_4)_3\cdot 3H_2O$; on the basis of fits to XANES and EXAFS data, the authors concluded that this complex was valence-localized. As reported above, our preparation of this complex, with triflate counterions, was found to lack observable electron hopping for $T < 240$ K.

We have previously shown[31,32] that one can determine the exchange coupling constant $J$ for antiferromagnetically coupled $Fe^{III}Fe^{III}$ complexes, provided that $J \leq 120$ cm$^{-1}$. More recently, Krebs and co-workers have used this method to determine $J$ for peroxodiferric reaction intermediates of ferritin and RNR.[44] We have determined $J$ here for diferric complex **3**, $J = 90 \pm 15$ cm$^{-1}$. This value compares favorably with that reported for another oxo/hydroxo bridged diferric complex, namely $[(6\text{-}Me_3\text{-}TPA)_2Fe_2(O)(OH)]^{3+}$ for which $J = 122$ cm$^{-1}$ was obtained from magnetic susceptibility studies.

**Acknowledgment.** Funding for this work was provided by NIH Grant GM-38767 to L.Q., NSF Grant MCB-9904421 to E.M., and an NSF graduate research fellowship to A.S.

**Supporting Information Available:** EPR spectra of polycrystalline **2** along with details regarding X-ray crystal structures of **1**, **2**, and **3**. This material is available free of charge via the Internet at http://pubs.acs.org.

IC030296K

(41) Gamelin, D. R.; Bominaar, E. L.; Kirk, M. L.; Wieghardt, K.; Solomon, E. I. *J. Am. Chem. Soc.* **1996**, *118*, 8085−8097.
(42) Dutta, S. K.; Ensling, J.; Werner, R.; Floerke, U.; Haase, W.; Gütlich, P.; Nag, K. *Angew. Chem., Int. Ed. Engl.* **1997**, *36*, 152−155.
(43) Hendrickson, D. N. In *NATO ASI Series C*; Kluwer Academic Publishers: Dordrecht, 1991; Vol. 343, pp 67−90.
(44) Krebs, C.; Bollinger, J. M., Jr.; Theil, E. C.; Huynh, B. H. *J. Biol. Inorg. Chem.* **2002**, *7*, 863−869.